

Journal of Materials Chemistry A

Accepted Manuscript



This is an *Accepted Manuscript*, which has been through the Royal Society of Chemistry peer review process and has been accepted for publication.

Accepted Manuscripts are published online shortly after acceptance, before technical editing, formatting and proof reading. Using this free service, authors can make their results available to the community, in citable form, before we publish the edited article. We will replace this *Accepted Manuscript* with the edited and formatted *Advance Article* as soon as it is available.

You can find more information about *Accepted Manuscripts* in the [Information for Authors](#).

Please note that technical editing may introduce minor changes to the text and/or graphics, which may alter content. The journal's standard [Terms & Conditions](#) and the [Ethical guidelines](#) still apply. In no event shall the Royal Society of Chemistry be held responsible for any errors or omissions in this *Accepted Manuscript* or any consequences arising from the use of any information it contains.

Cite this: DOI: 10.1039/c0xx00000x

www.rsc.org/xxxxxx

ARTICLE TYPE

Composite of Hierarchical Interpenetrating 3D Hollow Carbon Skeleton from Lotus Pollen and Hexagonal MnO₂ Nanosheets for High-Performance Supercapacitors

Hongpeng Li,^a Bin Wang,^a Xinyi He,^a Jun Xiao,^d Hongseng Zhang,^a Qi Liu,^a Jingyuan Liu,^a Jun Wang,^{* a,c} Lianhe Liu^c and Peng Wang^{*b}

Received (in XXX, XXX) Xth XXXXXXXXX 20XX, Accepted Xth XXXXXXXXX 20XX

DOI: 10.1039/b000000x

Numerous novel materials for next-generation energy storage and conversion devices have been prepared through simple and green methods to meet the urgent requirement for sustainable development. In this regard, lotus pollen, which is a cheap and common biomass waste, can be used as a potential carbon source for developing efficient electrode materials with a unique structure for high-performance supercapacitors. Following this aim, we successfully prepared hierarchical and interpenetrating three-dimensional (3D) hollow MnO₂/C composite via a facile and rapid dipping method, employing renewable, cost-effective and widespread natural porous lotus pollen as both the skeleton and carbon source. Benefiting from the synergistic effect between manganese dioxide and porous carbon matrix, the composite has a high specific capacitance of 257 F/g at a current density of 0.5 A/g and high energy density of 51.5 Wh/kg. In addition, the prepared composite exhibits good cycle stability even after 2000 charge/discharge cycles. The approach developed in this work directs the way to take full advantage of sustainable resources provided by nature, and opens up a novel route to design and prepare high-performance materials with greater potential application in high-performance energy storage systems.

Introduction

Appropriate sources of energy and their use are not only vital for economic development, but also provide basic security of a country's modernization plan for the improvement of living standards. The global climate warming, scarcity of resources and ecological environment become more and more serious with the development and progress of human society; as a result, human beings will pay more attention to solar, wind and other new, clean and renewable energy sources. However, the inherent characteristics of renewable energy (mainly wind and solar) determine power and energy output are often affected by seasons,

weather and geographical conditions. In addition, excess energy produced by renewable energy needs to be stored. To solve this problem, people must develop efficient energy storage devices. In many practical application fields, the most effective technologies for energy storage and conversion are fuel cells, batteries and supercapacitors.¹⁻⁴

Supercapacitors, also known as electrochemical capacitors (ECs), have attracted sizable attention because of their huge potential for application in portable electronic devices, hybrid electric vehicles and transportation, because they provide higher power densities than conventional batteries and possess reliable cycling stability.⁵⁻⁷ For example, in regard to safety and reliability, ECs are ready for large-scale application for the emergency doors of Airbus A380, pacemakers and airbags.¹ Generally speaking, supercapacitors are divided into two types according to the way they store energy: pseudo-capacitors (involving fast and reversible redox reactions) and electric double layer capacitors (EDLC, based on ion adsorption on the electrode surface).^{8,9} As with all other devices, performances of energy storage and conversion devices to a large extent depend on the materials they employ. Up to now, electrode materials can be divided into three classes: (1) carbon materials,^{10,11} which seem to be ideal materials for EDLC in terms of specific power and long cycle life; (2) transition metal oxides and hydroxides,¹²⁻¹⁷ which can provide higher power density and large specific capacitances due to Faradic reactions between electrode materials and ions; (3) conducting polymers.

^aKey Laboratory of Superlight Material and Surface Technology, Ministry of Education, College of Materials Science and Chemical Engineering, Harbin Engineering University, Harbin 150001, P. R. China

^bState Key Laboratory of Polymer Physics and Chemistry, Changchun Institute of Applied Chemistry, Chinese Academy of Sciences, Changchun 130022, P. R. China

^cInstitute of Advanced Marine Materials, Harbin Engineering University, Harbin 150001, P. R. China

^dCollege of Mechanical and Electrical Engineering, Harbin Engineering University, Harbin 150001, P. R. China

* Corresponding author: E-mail: zhqw1888@sohu.com; Fax: +86 451 8253 3026; Tel: +86 451 8253 3026

† Electronic Supplementary Information (ESI) available. See DOI: 10.1039/b000000x/

MnO₂ is widely regarded as one of the most promising materials for supercapacitors due to its low cost, high theoretical specific capacity and environmental friendliness. Nevertheless, a major problem is the poor conductivity of MnO₂ (10⁻⁵-10⁻⁶ S/cm), which hinders power performance and energy density, and limits its wide application in the field of energy storage.¹⁸ To effectively utilize MnO₂, efforts have been made to synthesize MnO₂/conductive matrix composite materials, for instance, MnO₂/Au,¹⁹ MnO₂/Zn₂SnO₄²⁰ and carbon/MnO₂.²¹ In the above various cases, MnO₂/C composite materials possess a huge potential for the next generation supercapacitors. Great efforts have been made to develop carbon-based materials that are identified as electrode materials for industrialization. Active carbon, graphene, carbon nanotubes and others have been used for commercial production. However, vast majority of them demand harsh synthetic process conditions. At present, the synthesis of carbon materials from organic biomass has attracted strong interest. Inspired by the abundant, renewable and economic biological materials with unique morphological structure and wonderful function characteristics, researchers have designed many novel multifunctional electrode materials by combining the advantages of bionics with traditional materials. Biswal et al. recently reported on functional microporous conducting carbon synthesized by dead plant leaves. This microporous carbon exhibited a relatively high specific capacitance of 400 F/g in aqueous 1 M H₂SO₄.²² Qian et al. prepared heteroatom doped porous carbon flakes by carbonizing human hair, which exhibited a specific capacitance of 340 F/g in 6 M KOH at a current density of 1 A/g.²³ Moreover, hollow porous MnO/C microspheres fabricated via a facile and green bio-template method yielded a specific capacity of 700 mAh/g at 0.1 A/g and gave outstanding cycling stability with 94% capacity retention.²⁴ Ren et al. prepared lightweight and high-performance MnO₂ loaded biomass carbonaceous aerogel composites via a facile hydrothermal carbonaceous procedure, and the MnO₂@AC composites displayed a specific capacitance of 123.5 F/g.²⁵ Apart from above mentioned materials, fungus, coconut shells, chicken eggshell membranes, fermented rice, wood, cornstalk, yogurt²⁶⁻³² and other biomass materials have been fully utilized for superior supercapacitor electrode materials.

With these in mind we successfully employed a green and facile rapid dipping method to synthesize hierarchical and interpenetrating 3D hollow MnO₂/C composite from natural porous lotus pollen grains as both the skeleton and carbon source, and to explore the potential of the electrode material for supercapacitors. As a common biomass material, pollen is relatively cheap and can be used as a potential carbon source. Furthermore, the majority of pollens have a unique porous surface formation to enable sufficient contact and reaction with the reagent. The structure, components and electrochemical performance of this material were fully characterized. Due to the unique hierarchical interpenetrating 3D hollow structure, the prepared MnO₂/C-3 composite possesses a high specific capacitance of 257 F/g at a current density of 0.5 A/g and high energy density of 51.5 Wh/kg. In addition, the MnO₂/C-3 composite exhibits good cycling stability, even after 2000 charge/discharge cycles.

Results and Discussion

The schematic illustration of the approach to fabricate hierarchical and interpenetrating 3D hollow MnO₂/C composite is shown in Scheme 1. As described in the experimental section (see Supporting Information), first, the protoplasm inside the pollen grains is removed by ethyl alcohol. Subsequently, 10 M H₂SO₄ solution is used as a dehydrant agent to pre-carbonize the pollen grains treated by alcohol (see Fig. 2). Then, pre-carbonation lotus pollen (PCLP) grains are dipped into KMnO₄ solution. In a pH neutral reaction system, the reaction between KMnO₄ and carbon can be described as Equation 1:³³



Insoluble MnO₂, formed via the above oxidation-reduction reaction, uniformly deposits onto the surface of the carbon-based material. And due to further growth, nano-granular manganese dioxide becomes hexagonal shaped. Finally, a hierarchical and interpenetrating 3D hollow MnO₂/C composite is produced by a simple calcining process under an inert atmosphere.

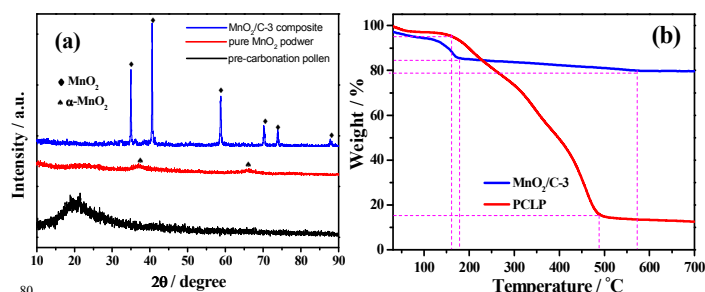
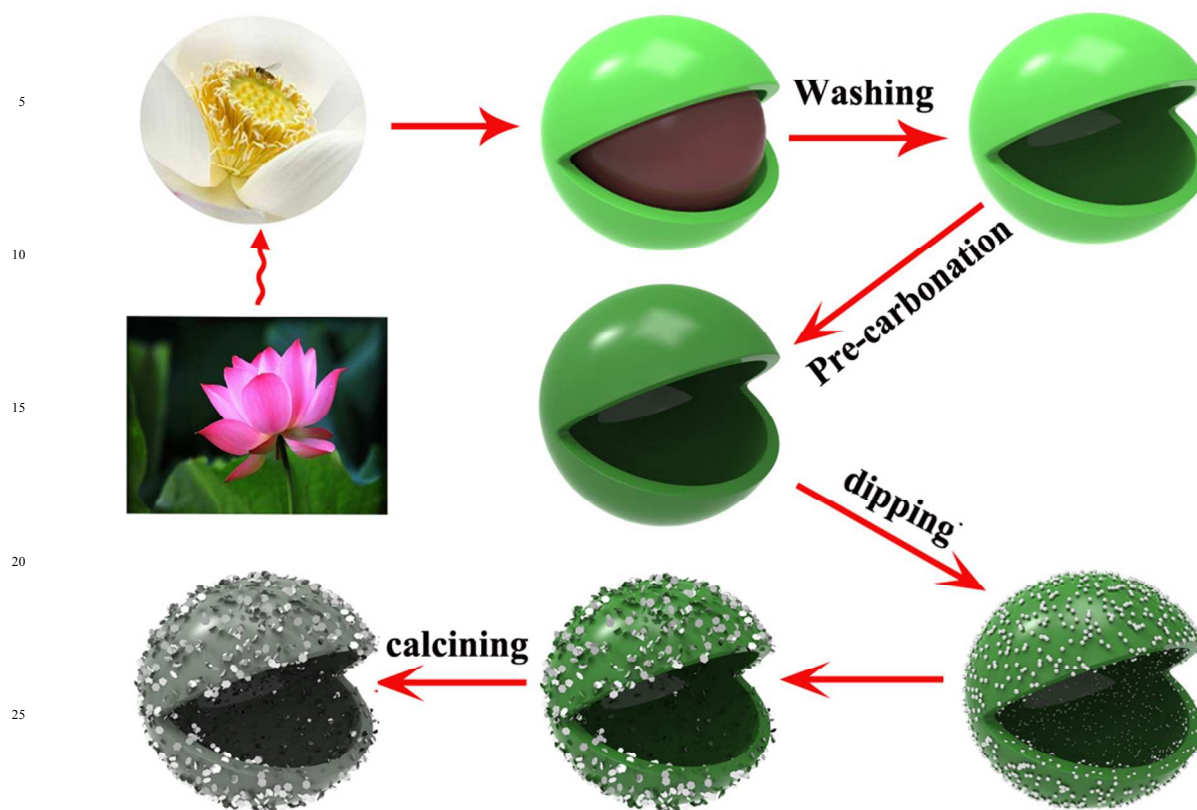


Fig. 1 (a): XRD patterns of the PCLP, MnO₂ powder and MnO₂/C-3 composite; (b) TGA curve of PCLP and MnO₂/C-3 composite.

Fig. 1 shows typical XRD patterns of the PCLP, pure MnO₂ powder and as prepared MnO₂/C-3 composite. A wide diffraction peak occurs at about 2θ = 20°, which shows the amorphous carbon structure of the PCLP.³⁴ Two weak diffraction peaks at 2θ angles of ~36.8 and 65.4 indicate the ramsdellite-type α-MnO₂ (JCPDS 44-0142) has poor crystallinity, which was prepared by reducing KMnO₄.³⁵ In addition, the as prepared MnO₂/C-3 composite shows clear characteristic peaks at 34.9°, 40.5°, 58.7°, 70.2°, 73.8° and 87.8°. These intense peaks are well indexed to the (111), (200), (220), (311), (222) and (400) planes of manganosite-type MnO₂ (JCPDS 07-0230). According to the Bragg equation, the interlayer spacings of (111), (200) and (220) crystal face are 0.26, 0.22 and 0.16 nm, respectively. Fig. 1(b) shows the TGA curves of MnO₂/C-3 composite and PCLP recorded in Ar. Water molecules in pollen grains depart around 170 °C. Nevertheless, about 77% weight loss has taken place from 180 °C to 490 °C because of the decomposition of organic components. The MnO₂/C-3 composite reveals 12% weight loss below 180 °C, which corresponds to a loss of physically adsorbed water and crystal water from the composite with no variation of the chemical valence. There is also only a 5.5% weight loss between 180 °C and 580 °C, which is due to the partial decomposition of organic components in pollen grains and the loss of oxygen from the MnO₂ lattice, leading to a phase transformation to Mn₂O₃.³⁶⁻³⁸ Potassium permanganate penetrates into the inner layer of the surface through holes and grooves on



Scheme 1 Schematic illustration of the approach to fabricate hierarchical interpenetrating 3D hollow MnO₂/C composite

the surface of the pollen, and, as a result, reacts with the outside and inside walls. The generated manganese dioxide tightly anchors onto the internal and external surfaces of the pollen by strong interaction,³⁹ and, most likely, prevents organic ingredients in pre-carbonation pollen grains largely decomposing at high temperature. Therefore, compared with pure pre-carbonation pollen, the weight loss of MnO₂/C-3 composite at high temperature is greatly reduced. In order to evaluate the value of MnO₂ to carbon ratio, thermal analysis was performed in O₂ atmosphere (Fig. S1). The ash content of PCLP is 12.91 wt %. Consequently, it can be calculated that the amount of MnO₂ in MnO₂/C-3 composite is about 62.89 wt %.

Fig. 2(a) shows the PCLP grain, a natural kind of porous material, is a spherical granule with a diameter of about 50 μm. There are many holes, brain corrugation-like folds and grooves on its surface. Pleated inner and outer walls, connecting with the columella layer, constitute the hierarchical porous hollow pollen grain (Fig. 2(b) and (c)). Fig. 2(d) presents high-magnified images of the smooth surface of the pre-carbonized pollen. Potassium permanganate solution infiltrates into the inner surface layer through these holes and grooves, effectively increasing the contact area between potassium permanganate and pollen wall. Hence, the utilization of the pollen grains will be greatly increased. Of particular significance is the way in which the hierarchical porous hollow structure accelerates the diffusion velocity of electrolyte ions and is, therefore, more conducive to the improvement of the electrochemical properties of electrode materials.⁴⁰

Figure 3 shows the hierarchical hexagonal MnO₂ uniformly coated on the inner and outer surfaces of the hollow porous

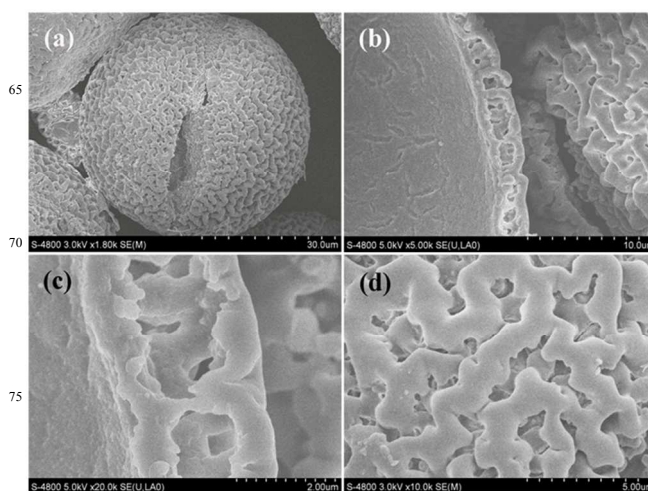


Fig. 2 FESEM images of PCLP grains: (a) low-magnification SEM images of an intact individual pollen grain; (b) a cross section, inside and outside surface of pollen grains; (c) and (d) high-magnified SEM images the surface of the pollen grain.

carbon spheres. Clearly, the hollow spherical structure of pollen grains does not collapse, and the surface morphology has not changed after calcination. It is noteworthy that hierarchical hexagonal MnO₂ nanosheets grow along the direction of folds and grooves onto the surface of pollen grains. Fig. 3(d) reveals the MnO₂ nanosheets have a special hexagonal construction with a side length of about 500 nm. It is well-known that the

interpenetrating 3D hollow structure is an ideal scaffold for preparation of monolithic composite electrodes; as a result, the special structure of MnO₂/C-3 composite increases the ion diffusion rate and increases the contact area between electrolyte and electrochemical active sites to improve the utilization of manganese dioxide.⁴¹ At the same time, electrons can be quickly transferred to MnO₂ nanoparticles that are strongly anchored onto the nanosheets by the underlying carbon skeleton. Therefore, the electrochemical properties of the overall MnO₂/C-3 composite are enhanced.³⁹ Typical TEM images in Fig. 3(e, f) clearly reveal that the hexagonal MnO₂ nanosheets possess an ultrathin morphology and include many small nanoplates (~30nm), the side lengths of which range from 500 nm to 1 μm. The insets are the corresponding HRTEM and SAED patterns of hierarchical hexagonal MnO₂. The marked lattice fringes (highlighted by the red lines) and diffraction rings (polycrystalline structure of as-prepared MnO₂) are consistent with the above-mentioned XRD results.

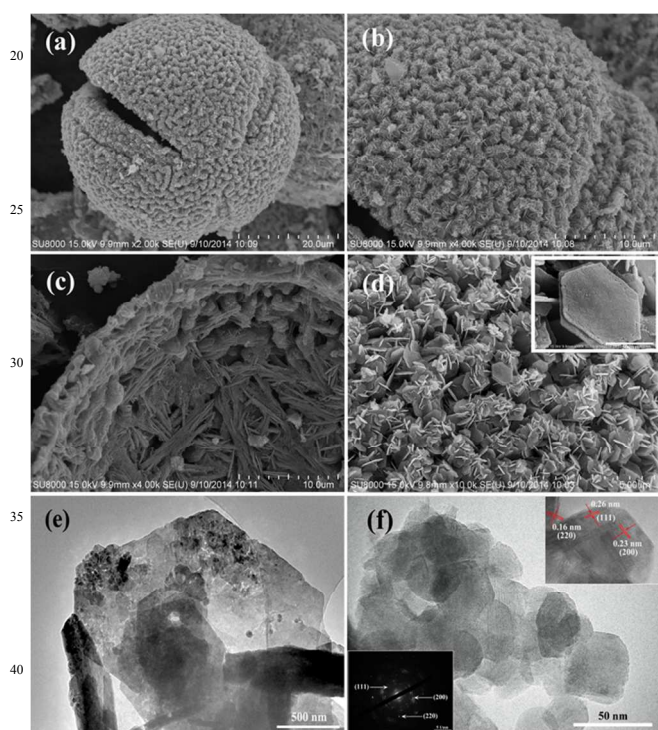


Fig. 3 Low- (a) and high- (b) magnified SEM images of MnO₂/C-3 composite; (c) the cross section image of a MnO₂/C-3 composite microsphere; (d) the magnified SEM image of hierarchical hexagonal MnO₂ nanosheets, and inset is of a corresponding enlarged image; (e, f) TEM image of MnO₂/C-3 composite under different magnifications, the inset is the corresponding HRTEM and SAED pattern of hierarchical hexagonal MnO₂.

Figure 4 shows the selected areas of SEM elemental mappings of MnO₂/C-3 composite and corresponding EDS spectra. The SEM elemental mappings of the selected red area in Figure 4(a) reveal a uniform distribution of C, O, Mn and K elements in the as-prepared MnO₂/C-3 composite. The corresponding EDS spectra (Fig. 4(b)) further demonstrate the basic chemical constitution of MnO₂/C-3 composite. It should be noted that the

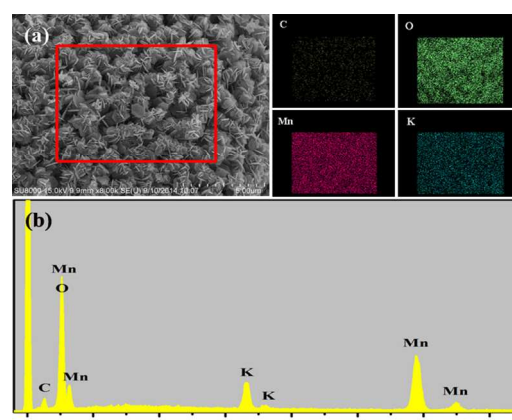


Fig. 4 (a) Selected areas of SEM elemental mappings of the MnO₂/C-3 composite and (b) corresponding EDS spectra.

oxygen functional groups on the surface of the sample can absorb electropositive K⁺ ions in the reactant due to the effect of electrostatic forces. As a result, there are still a small quantity of K elements in the composite.

The XPS spectra of the MnO₂/C-3 composite in Fig. 5(a) show that there are only three kinds of elements (Mn, O and C) present in the sample. Fig. 5(b) displays two characteristic peaks at 641.4 and 653.1 eV corresponding to the Mn 2p_{3/2} and Mn 2p_{1/2}, respectively. The binding energy separation is 11.7 eV, which indicates that manganese is present in 4+ oxidation states.^{23, 39, 42, 43} The XPS spectra of O 1s are shown in Fig. 5(c), which deconstruct into three components, indicating the presence of three types of oxygen-containing chemical bonds. The binding energy at 529.9 eV corresponds to the “oxygen” of Mn–O–Mn bond, while the band at 531.1 eV is attributed to Mn–O–H (hydroxide) and H–O–H (water molecule) at 532.3 eV.⁴⁴⁻⁴⁶ In addition, the high-resolution C 1s spectra (Fig. 5(d)) exhibit a sp² peak (C–C), which centers around 284.2 eV. The other two peaks at binding energies of 285.6 eV and 287.6 eV are typical features of carbon in a CH₃COH group containing the hydroxyl OH group and carbonyl or carboxylic groups (C=O).⁴⁷⁻⁵⁰

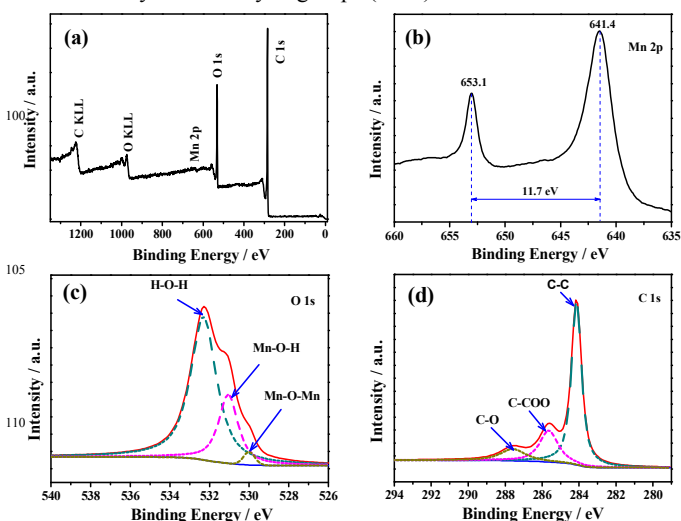


Fig. 5 (a) survey XPS spectra of MnO₂/C-3 composite; (b) Mn 2p XPS spectra; (c) XPS spectra of O 1s; (d) XPS spectra of C 1s.

Fourier transform infrared spectroscopy (FT-IR) further assists in understanding the construction of PCLP (Fig. 6a) and MnO₂/C-3 composite (Fig. 6b). The broad absorption bands around 3400 and 3310 cm⁻¹ are assigned to the stretching vibrations of O-H groups and bending vibrations of a small quantity of adsorbed water molecules.⁵¹ Compared with the pristine PCLP grains (Fig. 6a), the two absorption peaks (2920 and 2840 cm⁻¹) of composite (Fig. 6b) are obviously weakened, which demonstrate the surfaces of pollen grains have been covered by MnO₂.⁵² The observed peak at 1679 and 832 cm⁻¹ in Fig. 6a is ascribed to a stretching vibration of C=O and δ-CH.⁴³ Fig. 6b shows the bands at about 1405 cm⁻¹ are ascribed to C-H in-plane bending vibration.⁵³ And the presence of C-O bonds in various chemical surroundings has been shown to be within the 1300-950 cm⁻¹ range.⁵⁴ It should be noted that the 1630 and 1120 cm⁻¹ bands are normally ascribed to O-H bending vibrations combined with Mn atoms. In addition, two characteristic absorption peaks at 607 and 519 cm⁻¹ are observed in the MnO₂/C-3 composite, which are attributed to the Mn-O-Mn and Mn-O vibrations in [MnO₆] octahedral.^{52, 55, 56}

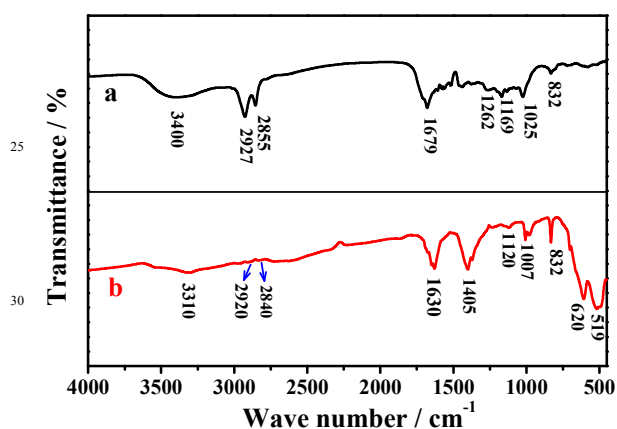
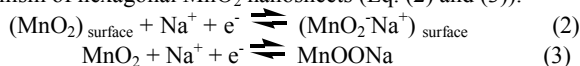


Fig. 6 FT-IR spectra of PCLP (a) and MnO₂/C-3 composite (b).

In this study, the electrochemical tests of carbonized lotus pollens (CLP), pure MnO₂ nanoparticles (the corresponding SEM images are presented in Fig. S2) and MnO₂/C-3 were tested in 1 M Na₂SO₄ solution (Fig. 7(a, b)). Obviously, compared with the pure MnO₂ nanoparticles and CLP, the CV curve of MnO₂/C-3 composite is expanded and quasi-rectangular in shape with highest current response. And the galvanostatic charge/discharge curve of MnO₂/C-3 composite is almost linear and symmetrical, demonstrating a rapid I-V response and an excellent electrochemical reversibility. The superior electrochemical performances of MnO₂/C-3 composite can benefit from the synergistic effects between electric double layer capacitive character of hollow carbon skeleton and pseudocapacitance mechanism of hexagonal MnO₂ nanosheets (Eq. (2) and (3)).^{57, 58}



Due to the porous hollow carbon skeleton can overcome the poor conductivity of MnO₂ (see Fig. S3), electrons can be quickly transmitted through carbon matrix to manganese oxide nanosheets. In addition, the flaky MnO₂ will increase the contact area with the electrolyte and provide a more convenient way to ion diffusion. The good interface contact among electrolyte,

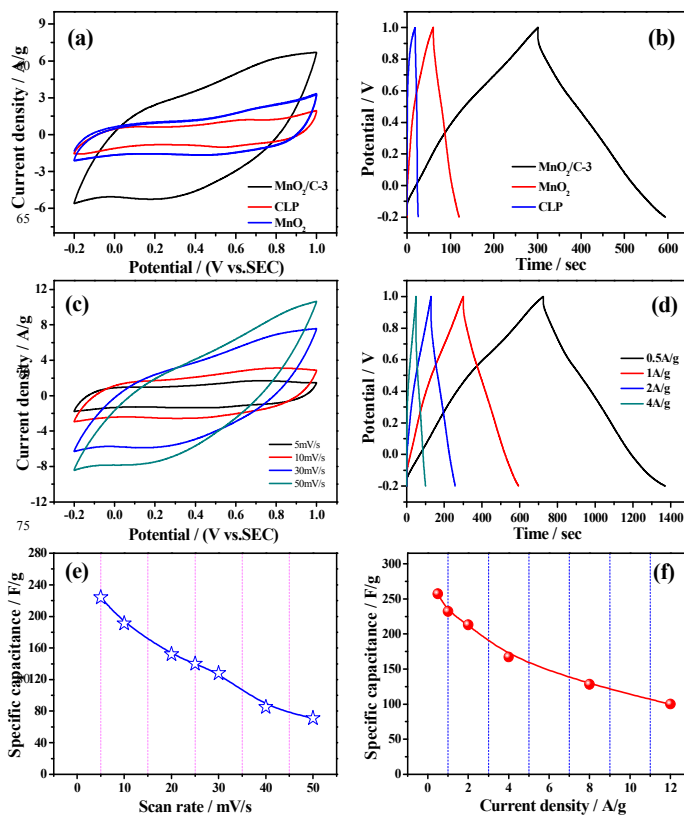


Fig. 7 A comparison of CV curves at 25 mV/s (a) and galvanostatic charge/discharge curves at a current density of 1 A/g (b) for pure MnO₂, CLP and MnO₂/C-3 composite.; (c, d) the CV and galvanostatic charge/discharge curves for MnO₂/C-3 composite at various scan rates; (e, f) the specific capacitance of MnO₂/C-3 at different scan rates and current densities in 1 M Na₂SO₄ solution.

MnO₂ nanosheets and porous carbon skeleton could facilitate the utilization of electrode; and, at the same time, improve overall electrochemical properties of the composite.³⁹ The CV curves for MnO₂/C-3 composite at various scan rates are shown in Fig. 7(c). All CV curves reveal a quasi rectangular shape in a wide potential range of -0.2 – 1.0 V, indicating ideal capacitive behavior for as-prepared electrode materials. It should be noted that a few Faradaic humps are revealed at ~0.3 V and 0.65 V in these CV curves, which are mainly attributed to the reversible redox reactions of the heteroatom²⁴ (sulphur atoms on the surface of pre-carbonized pollen grains, see Fig. S4 and Table. S1) and oxygen functional groups.⁵⁹ Based on Gogotsi and Zheng,^{1, 60} the presence of small amounts of oxygen-containing functional groups are of benefit for enhancing the wettability and cycling stability of the carbonaceous materials. The capacitive performances for MnO₂/C-3 were further measured by galvanostatic charge/discharge experiments. Fig. 7(d) reveals typical galvanostatic charge/discharge curves of MnO₂/C-3 at various current densities. All of the galvanostatic charge/discharge curves are quasi-symmetrical and with no obvious iR drops in the total potential range. The specific capacitance values of MnO₂/C-3 at different scan rates and current densities are shown in Fig. 7(e) and (f). The specific capacitance calculated from CV curves is from 224 to 71 F/g as

the scan rates increase from 5 to 50 mV/s. This is because electrolyte ions can take full advantage of most electrochemical active sites (MnO_2 nanosheets located in the inner and outer surfaces of hollow porous carbon skeleton) at low scan rates. Whereas, at higher scan rates, the movement of electrolyte ions (Na^+ ions and protons) is limited by a time constraint, and only the outer electroactive surface can be utilized for charge storage.⁶¹ Then, the highest specific capacitance value obtained from discharge time is 257 F/g at 0.5 A/g. Nevertheless, because of fast charging limits the diffusion of electrolyte ions onto the electrode surface at high current densities,³⁹ the specific capacitance decreases with the increase of current density. The outstanding electrochemical performance is higher than those of hollow $\epsilon\text{-MnO}_2$ spheres (115 F/g),⁶² carbon microsphere/ MnO_2 composite (181 F/g),⁶³ core-shell $\text{MnO}_2\text{-MnO}_2/\text{C}$ composite (203 F/g)⁶⁴ and most reported carbon, biomass derived carbon or biomass derived carbon/ MnO_2 composites based materials (Table S2). This satisfactory result demonstrates its potential application for high-performance supercapacitors. Moreover, the products of different reaction time (the corresponding SEM images are presented in Fig. S5) were also tested under the same conditions (Fig. S6(a, b)). Compared with other products, the significantly better electrochemical performances of $\text{MnO}_2/\text{C-3}$ may benefit from the complete and unique structure of the $\text{MnO}_2/\text{C-3}$ composite.

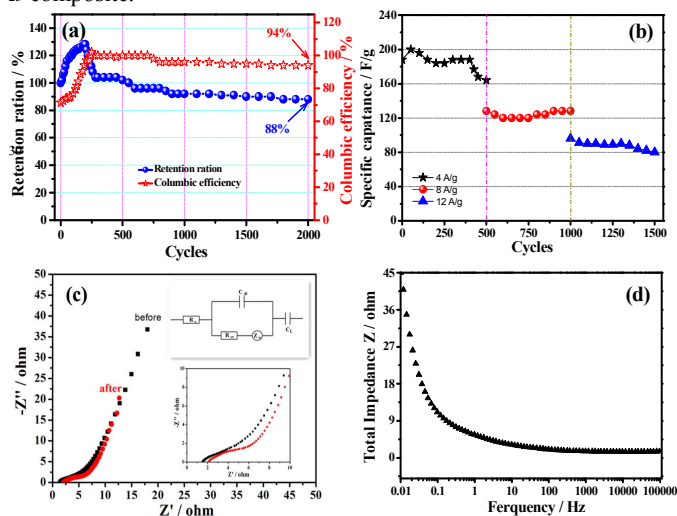


Fig. 8 Cycling performance of $\text{MnO}_2/\text{C-3}$ composite in 1 M Na_2SO_4 aqueous solution (a) at a current density of 4 A/g for 2000 cycles and (b) at progressively varied current densities; (c) Nyquist plots of $\text{MnO}_2/\text{C-3}$ electrode before and after 2000 cycles, top right inset shows the electrical equivalent circuit and bottom right is the magnified high frequency region of the plots; (d) evolution of total impedance vs. frequency before 2000 cycles.

Apart from high specific capacitance, long cycle life or cycle stability is also an important parameter for supercapacitors. Fig. 8(a) shows the capacitance retention ratio and Coulombic efficiency of $\text{MnO}_2/\text{C-3}$ composite electrode as a function of cycle numbers. The enhanced capacity in the first two hundred cycles may be due to the improvement of ion accessibility in 3D porous hollow carbon skeleton structure during the cycling procedure. Furthermore, electrode materials may also be activated

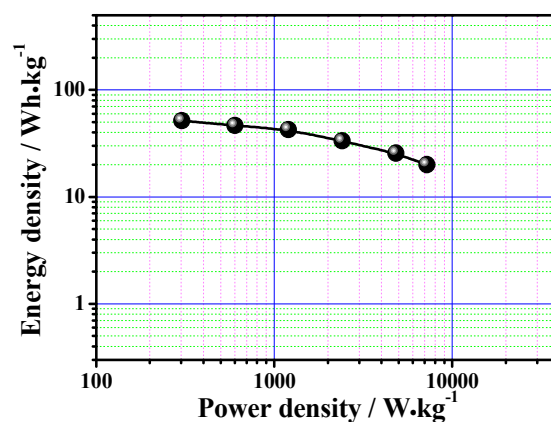


Fig. 9 Ragone plot of the as-prepared $\text{MnO}_2/\text{C-3}$ composite.

by long term high current density. The specific capacitance still retains 88% of its maximum after 2000 cycles, which shows that this $\text{MnO}_2/\text{C-3}$ composite electrode possesses excellent stability. Moreover, the coulombic efficiency remains as high as 94% after 2000 continuous cycles. This outstanding electrochemical stability is attributed to the hollow carbon skeleton preventing the possible volume change during long-time cycling.⁶⁵ Fig. 8(b) presents cycle performance of $\text{MnO}_2/\text{C-3}$ composite at progressively varying current densities. When the current density increases from 4 A/g to 12 A/g, the specific capacitances remain relatively stable and decrease regularly with a gradually enlarged current density; it means that the $\text{MnO}_2/\text{C-3}$ composite possesses excellent cycle stability after the electrode is subjected to sudden current density change. The electrochemical impedance spectroscopy (EIS) of the $\text{MnO}_2/\text{C-3}$ composite was measured in the frequency range of 100 kHz to 0.01 Hz at the open circuit potential with an ac perturbation of 5 mV. Fig. 8(c) shows the Nyquist plots of $\text{MnO}_2/\text{C-3}$ electrode before and after 2000 cycles. The curves reveal a representative hybrid control process: an electrode reaction kinetics control (charge transfer process) at high frequency region and diffusion control at low frequency region.⁶⁶ The as shown impedance spectra are nearly similar in form with an arc at high frequency region and an almost vertical straight line parallel to the imaginary axis (Z'') at low frequency region. The electrical equivalent circuit presented in the top right corner is made up of R_s , C_{dl} , R_{ct} , Z_w and C_L . R_s is the combined resistance of intrinsic resistance of substrate, ionic resistance of electrolyte and contact resistance at the active material/current collector interface. C_{dl} is the double-layer capacitance of the composite. R_{ct} is the charge transfer resistance at the interface between electrode and electrolyte. Z_w is the Warburg resistance, which is the result of the frequency dependence of electrolyte ion diffusion/transport to the electrode surface. And, C_L is the capacitance limit.^{27, 39, 67} The R_s of electrode increases from 1.6 to 2.4 Ω . Only a slightly increase occurs in R_{ct} from 1.4 to 2.1 Ω after 2000 cycles, which may be caused by the consumption of electrochemical active sites. Fig. 8(d) shows the relationship between total impedance (Z) and frequency before 2000 cycles. At low frequency region, electrolyte ions attempt to penetrate deeper into the electrode by passing through the random stacking of the MnO_2 nanosheet layers and porous carbon skeleton. Hence, the resistive and the capacitive behavior can lead to higher

impedance. The electrolyte ion penetration path decreases with the increase of frequency. That means that the impedance reduces at the high frequency region, which is consistent with the results shown in the Fig. 8(c).^{22, 68, 69} These results, once again, demonstrate the excellent electrochemical performance of MnO₂/C-3 composite.

To further demonstrate the operable electrochemical characteristics, the energy density (E) and power density (P) of the as-prepared MnO₂/C-3 composite were calculated from the charge/discharge curves at different current densities and are given in the Ragone plot (Fig. 9). It can be clearly seen that the MnO₂/C-3 composite based electrode with a wide operating voltage of 1.2 V exhibits an energy density of 51.5 Wh/kg at a power density of 303 W/kg and still maintains 20 Wh/kg at a high power density of 7200 W/kg in 1 M Na₂SO₄ aqueous solution. The high energy density in this study are not only comparable to those MnO₂-based composite supercapacitors,^{70, 71} but also higher than most of the biomass-based supercapacitors.^{27, 72-74}

The superior electrochemical performance can benefit from the unique hierarchical nanostructure of MnO₂/C-3 composite: (1) The anisotropic morphology and hollow spherical structure create fast diffusion paths for the electrolyte ion, to enhance ion transmission and facilitate the utilization of electrode; (2) Well-dispersed MnO₂ nanosheets can shorten the diffusion path of electrolyte ions and ensure a high electrochemical utilization of MnO₂; (3) The porous and carbon skeleton in the composite serves as a support for the deposition of MnO₂ nanosheets; at the same time, it can enhance the overall conductivity of the material and reduce the charge transfer resistance; (4) The unique stable hollow 3D geometric construction may prevent a possible volume change during the charge/discharge procedures and result in outstanding cycling stability.

Conclusions

Overall, our present work provides a novel, facile and cost-effective strategy to prepare hierarchical 3D MnO₂/C composite by using renewable, green and widespread natural porous lotus pollen grains as both the skeleton and carbon source. This MnO₂/C composite was produced via a simple methodology involving a pre-treatment and a rapid dipping process. We found that the dipping time has a significant influence on the morphology and electrochemical performance of the final products. After dipping the metal oxide/carbon material in KMnO₄ solution for 3 h, the unique hierarchical hollow 3D structure exhibits high specific capacitance and an energy density of 257 F/g and 51.5 Wh/kg, respectively. The synergistic effect between carbon matrix and manganese dioxide enhances double layer and pseudocapacitive contributions. At the same time, the porous hollow carbon skeleton not only serves as a support for the deposition of MnO₂ nanosheets, but also improves the electrical connectivity among MnO₂ nanosheets. Moreover, the MnO₂/C-3 composite exhibits good cyclic stability even after 2000 charge/discharge cycles. We believe that the facile, green and economical method presented in this work will set a good example for taking full advantage of sustainable resources provided by nature, opening up a novel route to design and prepare high-performance materials with great potential application in high-performance energy storage systems.

Acknowledgments

This work was supported by National Natural Science Foundation of China (21353003), Special Innovation Talents of Harbin Science and Technology (2013RFQXJ145), Fundamental Research Funds of the Central University (HEUCFZ), Natural Science Foundation of Heilongjiang Province (B201316), Program of International S&T Cooperation special project (2013DFA50480), and the fund for Transformation of Scientific and Technological Achievements of Harbin (2013DB4BG011), Research and Development of Industrial Technology Project of Jilin Province (JF2012C022-4).

References

- 1 P. Simon and Y. Gogotsi, *Nat. Mater.*, 2008, **7**, 845.
- 2 C. Largeot, C. Portet, J. Chmiola, P. Taberna, Y. Gogotsi and P. Simon, *J. Am. Chem. Soc.*, 2008, **130**, 2730.
- 3 S. Kandalkar, D. Dhawale, C. Kim and C. Lokhande, *Synth. Met.*, 2010, **160**, 1299.
- 4 X. Xiao, T. Q. Li, Z. H. Peng, H. Y. Jin, Q. Z. Zhong, Q. Y. Hu, B. Yao, Q. P. Luo, C. F. Zhang, L. Gong, J. Chen and Y. Gogotsi, *J. Zhou, Nano Energy*, 2014, **6**, 1.
- 5 J. R. Miller and P. Simon, *Science*, 2008, **321**, 651.
- 6 Y. P. Zhai, Y. Q. Dou, D. Y. Zhao, P. F. Fulvio, R. T. Mayes and S. Dai, *Adv. Mater.*, 2011, **23**, 4828.
- 7 X. H. Lu, M. H. Yu, G. M. Wang, Y. X. Tong and Y. Li, *Energy Environ. Sci.*, 2014, **7**, 2160.
- 8 P. Simon, Y. Gogotsi and B. Dunn, *Science*, 2014, **343**, 1210.
- 9 Z. M. Hu, X. Xiao, C. Chen, T. Q. Li, L. Huang, C. F. Zhang, J. Su, L. Miao, J. J. Jiang, Y. R. Zhang and J. Zhou, *Nano Energy*, 2015, **11**, 226.
- 10 E. Frackowiak, S. Delpeux, K. Jurewicz, K. Szostak, D. Cazorla-Amoros and F. Be guin, *Chem. Phys. Lett.*, 2002, **361**, 35.
- 11 V. Ruiz, C. Blanco, E. R. Pin˜ero, V. Khomeiko, F. Be'guin and R. Santamar'a, *Electrochim. Acta*, 2007, **52**, 4969.
- 12 Y. R. Ahn, M. Y. Song, S. M. Jo and C. R. Park, *Nanotechnology*, 2006, **17**, 2865.
- 13 C. C. Hu, Y. H. Huang and K. H. Chang, *J. Power Sources*, 2002, **108**, 117.
- 14 J. Yan, T. Wei, J. Cheng, Z. J. Fan and M. L. Zhang, *Mater. Res. Bull.*, 2010, **45**, 210.
- 15 P. A. Nelson and J. R. Owen, *J. Electrochem. Soc.*, 2003, **150**, 1313.
- 16 S. G. Kandalkar, J. L. Gunjakar and C. D. Lokhande, *Appl. Surf. Sci.*, 2008, **254**, 5540.
- 17 M. Nakayama, A. Tanaka, Y. Sato, *Langmuir*, 2005, **21**, 5907.
- 18 A. E. Fischer, K. A. Pettigrew, D. R. Rolison, R. M. Stroud and J. W. Long, *Nano Lett.*, 2007, **7**, 281.
- 19 X. Y. Lang, A. Hirata, T. Fujita and M. W. Chen, *Nat. Nanotechnology*, 2011, **6**, 232.
- 20 L. H. Bao, J. F. Zhang and X. D. Li, *Nano Lett.*, 2011, **11**, 1215.
- 21 Q. Li, X. F. Lu, H. Xu and Y. X. Tong, G.R. Li, *ACS Appl. Mater. Interfaces*, 2014, **6**, 2726.
- 22 M. Biswal, A. Banerjee, M. Deo and S. Ogale, *Energy Environ. Sci.*, 2013, **6**, 1249.
- 23 W. J. Qian, F. X. Sun, Y. H. Xu, L. H. Qiu, C. H. Liu, S. D. Wang and F. Yan, *Energy Environ. Sci.*, 2013, **7**, 379.
- 24 Y. Xia, Z. Xiao, X. Dou, H. Huang, X. H. Lu, R. J. Yan, Y. P. Gan, W. J. Zhu, J. P. Tu, W. K. Zhang and X. Y. Tao, *ACS Nano*, 2013, **7**, 7083.
- 25 Y. M. Ren, Q. Xu, J. M. Zhang, H. X. Yang, B. Wang, D. Y. Yang, J. H. Hu and Z. M. Liu, *ACS Appl. Mater. Interfaces*, 2014, **6**, 9689.
- 26 C. L. Long, X. Chen, L. L. Jiang, L. J. Zhi and Z. J. Fan, *Nano Energy*, 2015, **12**, 141.
- 27 L. Sun, C. G. Tian, M. T. Li, X. Y. Meng, L. Wang, R. H. Wang, J. Yin and H. G. Fu, *J. Mater. Chem. A*, 2013, **1**, 6462.
- 28 Z. Li, L. Zhang, B. S. Amirkhiz, X. H. Tan, Z. W. Xu, H. L. Wang, B. C. Olsen, C. M. B. Holt and D. Mitlin, *Adv. Energy Mater.*, 2012, **2**, 431.

- 29 S. Y. Gao, Y. L. Chen, H. Fan, X. J. Wei, C. G. Hu, H. X. Luo and L. T. Qu, *J. Mater. Chem. A*, 2014, **2**, 3317.
- 30 A. Cuna, N. Tancredi, J. Bussi, V. Barranco, T. A. Centeno, A. Quevedo and J. M. Rojo, *J. Electrochem. Soc.*, 2014, **161**, A1806.
- 31 L. Wang, G. Mu and C. G. Tian, *ChemSusChem*, 2013, **6**, 880.
- 32 M. Wahid, G. Parte, D. Phasec and S. Ogale, *J. Mater. Chem. A*, 2015, **3**, 1208.
- 33 X. B. Jin, W. Z. Zhou, S. W. Zhang and George Z. Chen, *Small*, 2007, **3**, 1513.
- 34 Y. Wang, Z. M. Liu, B. X. Han, Y. Huang and G. Y. Yang, *Langmuir*, 2005, **21**, 10846.
- 35 H. Pang, S. M. Wang, G. C. Li, Y. H. Ma, J. Li, X. X. Li, L. Zhang, J. S. Zhang and H. H. Zheng, *J. Mater. Chem. A*, 2013, **1**, 5053.
- 36 S. Franger, S. Bach, J. Farcy, J. P. Pereira-Ramos and N. Baffier, *J. Power Sources*, 2002, **109**, 262.
- 37 S. Devaraj and N. Munichandraiah, *J. Solid State Electrochem.*, 2008, **12**, 207.
- 38 Y. Munaiah, B. G. S. Raj, T. P. Kumar and P. Ragupathy, *J. Mater. Chem. A*, 2013, **1**, 4300.
- 39 Z. J. Fan, J. Yan, T. Wei, L. J. Zhi, G. Q. Ning, T. Y. Li and F. Wei, *Adv. Funct. Mater.*, 2011, **21**, 2366.
- 40 L. Qie, W. M. Chen, H. H. Xu, X. Q. Xiong, Y. Jiang, F. Zou, X. H. Hu, Y. Xin, Z. L. Zhang and Y. H. Huang, *Energy Environ. Sci.*, 2013, **6**, 2497.
- 41 S. Vijayakumar, S. Nagamuthu and G. Muralidharan, *ACS Sustainable Chem. Eng.*, 2013, **1**, 1110.
- 42 X. H. Lu, D. Z. Zheng, T. Zhai, Z. Q. Liu, Y. Y. Huang, S. L. Xie and Y. X. Tong, *Energy Environ. Sci.*, 2011, **4**, 2915.
- 43 B. Wang, X. Y. He, H. P. Li, Q. Liu, J. Wang, L. Yu, H. J. Yan, Z. S. Li and P. Wang, *J. Mater. Chem. A*, 2014, **2**, 12968.
- 44 M. Chigane and M. Ishikawa, *J. Electrochem. Soc.*, 2000, **147**, 2246.
- 45 M. Chigane, M. Ishikawa and M. Izaki, *J. Electrochem. Soc.*, 2001, **148**, D96.
- 46 C. C. Hu and T. W. Tsou, *Electrochim. Acta.*, 2002, **47**, 3523.
- 47 K. Karthikeyan, S. Amaresh, S. N. Lee, X. L. Su, V. Aravindan, Y. G. Lee and Y. S. Lee, *ChemSusChem*, 2014, **7**, 1435.
- 48 D. W. Wang, A. J. Du, E. Taran, G. Q. (Max) Lu and I. R. Gentle, *J. Mater. Chem.*, 2012, **22**, 21085.
- 49 X. D. Qi, T. N. Zhou, S. Deng, G. Y. Zong, X. L. Yao and Q. Fu, *J. Mater. Sci.*, 2014, **49**, 1785.
- 50 N. Kuma and R. Ramadoss, *J. Phys. D: Appl. Phys.*, 2013, **46**, 275501.
- 51 A. Ramadoss and S. J. Kim, *Mater. Chem. Phys.*, 2013, **140**, 405.
- 52 X. F. Xie and L. Gao, *Carbon*, 2007, **45**, 2365.
- 53 Y. M. Ren, Q. Xu, J. M. Zhang, H. X. Yang, B. Wang, D. Y. Yang, J. H. Hu and Z. M. Liu, *ACS Appl. Mater. Interfaces*, 2014, **6**, 9689.
- 54 C. Luo, R. Y. Wei, D. Guo, S. F. Zhang and S. Q. Yan, *Chem. Eng. J.*, 2013, **225**, 406.
- 55 A. B. Yuan, Q. L. Zhang, *Electrochem. Commun.*, 2006, **8**, 1173.
- 56 L. C. Tan, J. Wang, Q. Liu, Y. B. Sun, X. Y. Jing, L. H. Liu, J. Y. Liu and D. L. Song, *New J. Chem.*, 2014, **D10**: 10.1039/c4nj01256a.
- 57 M. Toupin, T. Brousse and D. Be'anger, *Chem. Mater.*, 2004, **16**, 3184.
- 58 Y. Munaiah, B. G. S. Raj, T. P. Kumar and P. Ragupathy, *J. Mater. Chem. A*, 2013, **1**, 4300.
- 59 Z. Jin, X. D. Yan, Y. H. Yu and G. J. Zhao, *J. Mater. Chem. A*, 2014, **2**, 11706.
- 60 G. Y. Zheng, L. B. Hu, H. Wu, X. Xie and Y. Cui, *Energy Environ. Sci.*, 2011, **4**, 3368.
- 61 Z. J. Lao, K. Konstantinov, Y. Tournaire, S. H. Ng, G. X. Wang and H. K. Liu, *J. Power Sources*, 2006, **162**, 1451.
- 62 D. D. Han, X. Y. Jing, P. C. Xu, Y. S. Ding and J. Y. Liu, *J. Solid State Chem.*, 2014, **218**, 178.
- 63 X. X. Zhang, F. Ran, H. L. Fan, Y. T. Tan, L. Zhao, X. M. Li, L. B. Kong and L. Kang, *J. Energy Chem.*, 2014, **23**, 82.
- 64 X. M. Zhang, J. Ma, W. L. Yang, Z. Gao, J. Wang, Q. Liu, J. Y. Liu and X. Y. Jing, *CrystEngComm*, 2014, **16**, 4016.
- 65 F. Chen, W. J. Zhou, H. F. Yao, P. Fan, J. T. Yang, Z. D. Fei and M. Q. Zhong, *Green Chem.*, 2013, **15**, 3057.
- 66 B. Wang, Q. Liu, J. Han, X. F. Zhang, J. Wang, Z. S. Li, H. J. Yan and L. H. Liu, *J. Mater. Chem. A*, 2014, **2**, 1137.
- 67 H. C. Gao, F. Xiao, C. B. Ching and H. W. Duan, *ACS Appl. Mater. Interfaces*, 2012, **4**, 2801.
- 68 J. G. Lee, J. Y. Kima, S. H. Kim, *J. Power Sources*, 2006, **160**, 1495.
- 69 D. Puthusseri, V. Aravindan, S. Madhavid and S. Ogale, *Energy Environ. Sci.*, 2014, **7**, 728.
- 70 Z. S. Wu, W. C. Ren, D. W. Wang, F. Li, B. L. Liu and H. M. Cheng, *ACS Nano*, 2010, **4**, 5835.
- 71 Q. Cheng, J. Tang, J. Ma, H. Zhang, N. Shinya and L. C. Qin, *Carbon*, 2011, **49**, 2917.
- 72 C. Peng, J. W. Lang, S. Xu, X. L. Wang, *RSC Adv.*, 2014, **4**, 54662.
- 73 S. Nagamuthu, S. Vijayakumar and G. Muralidharan, *Ind. Eng. Chem. Res.*, 2013, **52**, 18262.
- 74 X. J. He, P. H. Ling, J. S. Qiu, Mo. Yu, X. Y. Zhang, C. Yu and M. D. Zheng, *J. Power Sources*, 2013, **240**, 109.